Research Square

Preprints are preliminary reports that have not undergone peer review.
They should not be considered conclusive, used to inform clinical practice,
or referenced by the media as validated information.

A low-cost direct-conversion CZT gamma camera for planar thyroid scintigraphy: detector characterisation and clinical demonstration against a commercial NaI(Tl) system

Koushik V
Sri Sathya Sai Institute of Higher Learning
Vishal Rao
HCG Cancer Centre
Murali Ravi
muraliravi@sssihl.edu.in

Sri Sathya Sai Institute of Higher Learning

Article

Keywords: Cadmium zinc telluride, direct-conversion detector, small field-of-view gamma camera, thyroid scintigraphy, energy resolution, dual-isotope imaging

Posted Date: November 16th, 2026

DOI: https://doi.org/10.21203/rs.3.rs-11529171/v1

License: This work is licensed under a Creative Commons Attribution 4.0 International License.
Read Full License

Additional Declarations: No competing interests reported.

A low-cost direct-conversion CZT gamma camera for planar thyroid scintigraphy: detector characterisation and clinical demonstration against a commercial NaI(Tl) system

Koushik V[1], Vishal Rao[2], Murali Ravi[1]*
[1] Department of Physics, Sri Sathya Sai Institute of Higher Learning, Puttaparthi, Andhra Pradesh, India
[2] HCG Cancer Centre, Bengaluru, Karnataka, India
*Corresponding author: Murali Ravi (muraliravi@sssihl.edu.in)

Abstract

Direct-conversion cadmium zinc telluride (CZT) detectors have well-documented advantages over the sodium iodide (NaI(Tl))/photomultiplier cameras still standard in clinical gamma imaging, but low-cost, indigenously developed CZT systems are seldom characterised in detail. We characterise the detector physics of one such camera, a portable Small Area Imaging Gamma Camera (SAIGC; 44×44 pixellated CZT array, 2×2×5 mm elements, 88×88 mm field of view), and benchmark it against a commercial GE Infinia NaI(Tl) system for planar thyroid scintigraphy. Thirty patients referred for ^{99m}Tc-pertechnetate scintigraphy were imaged on both systems, with every SAIGC figure derived from raw list-mode data and compared with the published NEMA NU-1 specifications of GE Infinia. Energy resolution was 3.52% full width at half maximum at 140 keV, against 9.8% for GE Infinia. Separately, clinical pixel counts followed Poisson statistics on short timescales, with no detectable correlated counting from the electronics. Median acquisition time was 119.6 s per view. Bench source and phantom studies showed spatial discrimination, simultaneous dual-isotope imaging (^{152}Eu/^{99m}Tc, only 18 keV apart) and thyroid morphology preserved over a full 0–360° n, indicating single-photon emission computed tomography (SPECT) feasibility. The camera delivers these detector-level gains, alongside clinically interpretable images, at roughly one-tenth the cost.

Keywords: Cadmium zinc telluride; direct-conversion detector; small field-of-view gamma camera; thyroid scintigraphy; energy resolution; dual-isotope imaging.

Introduction

Planar thyroid scintigraphy with ^{99m}Tc-pertechnetate remains a routine functional investigation for goitre, thyroiditis, hyper- and hypofunctioning nodules and Graves' disease. The majority of these studies are performed on large field-of-view gamma cameras, comprising a monolithic slab of NaI(Tl) read out by an array of photomultiplier tubes in the Anger configuration [1]. Such cameras resolve spatial detail only to approximately 7–11 mm and are bulky and stationary [2], typically requiring a dedicated, purpose-built imaging suite [3], which renders them poorly suited to small-organ, bedside or intraoperative imaging.

This limitation has motivated an extensive body of work on compact, small field-of-view and handheld cameras for dedicated small-organ and intraoperative applications, among them sentinel-lymph-node localisation and minimally invasive parathyroid surgery [4–8]. Early portable scintillation cameras [4]

were succeeded by position-sensitive-PMT and CCD-coupled scintillator detectors [9], and subsequently by direct-conversion semiconductors. Cadmium telluride (CdTe) and cadmium zinc telluride (CZT) convert an incident γ-photon directly into charge, obviating the intermediate scintillation-to-photodetection stage; they afford superior energy resolution, operate at room temperature and occupy a compact volume, and have been deployed in handheld and organ-specific cameras [10–14]. Improved energy resolution is not merely an incremental gain: it narrows the photopeak acceptance window and thereby rejects a greater fraction of Compton-scattered photons [15], and scatter rejection is a principal determinant of image contrast in the scatter-dominated geometries characteristic of clinical imaging [16,17].

Conventional gamma cameras detect photons indirectly: a NaI(Tl) scintillator converts an absorbed gamma ray into visible light, which a photomultiplier array then converts into charge. Each conversion adds statistical broadening, and the resulting energy resolution is typically near 9–10% FWHM at 140 keV. CZT, by contrast, is a direct-conversion semiconductor: an absorbed photon generates electron hole pairs that are collected directly by pixellated electrodes, eliminating the optical stage entirely [18,19]. Because the mean energy required to create a charge carrier is roughly an order of magnitude smaller than the energy required to produce a detectable scintillation photoelectron, the primary signal carries far more information carriers per keV, and the achievable energy resolution improves correspondingly, to a few per cent FWHM at 140 keV [18,20,21].

Three material properties make CZT well matched to single-photon emission imaging. Its wide bandgap (≈1.57 eV) suppresses thermally generated leakage current and permits room-temperature operation without cryogenics [19,20]. Its high effective atomic number and density (≈5.8 g cm^{-3}) give strong photoelectric absorption at the 140 keV of ^{99m}Tc in a crystal only millimetres thick [19,22]. And because the detector is intrinsically pixellated by its electrode pattern rather than by an Anger-logic position estimate, spatial sampling is set by the anode pitch, decoupling spatial resolution from the light-spreading and photomultiplier statistics that limit scintillator cameras [21,23].

The principal engineering difficulty of CZT is charge transport: holes are far less mobile than electrons and are readily trapped, so the collected signal depends on interaction depth. The standard remedy is the small-pixel effect, in which the anode is made small relative to the detector thickness so that the induced signal is dominated by electron motion in the immediate vicinity of the anode, largely removing the depth dependence [23]. Combined with per-pixel energy calibration, this recovers a clean photopeak from a pixellated array. Direct-conversion CZT cameras exploiting these principles are now established clinically, notably in dedicated cardiac SPECT and in small field-of-view and intraoperative systems, where their energy resolution, compactness and room-temperature operation are decisive [21,24,25]. Cost and crystal-scale uniformity, rather than physics, remain the principal barriers to wider adoption [20,21], which motivates the detailed characterisation of an affordable, indigenously developed CZT camera reported here.

The Small Area Imaging Gamma Camera (SAIGC) was developed against this background at Sri Sathya Sai Institute of Higher Learning: a portable, pixellated-CZT camera intended to deliver high-resolution functional imaging at low cost and in a compact footprint [26]. Our prior publications have detailed its detector, acquisition electronics, reconstruction pipeline and FPGA-accelerated tomographic

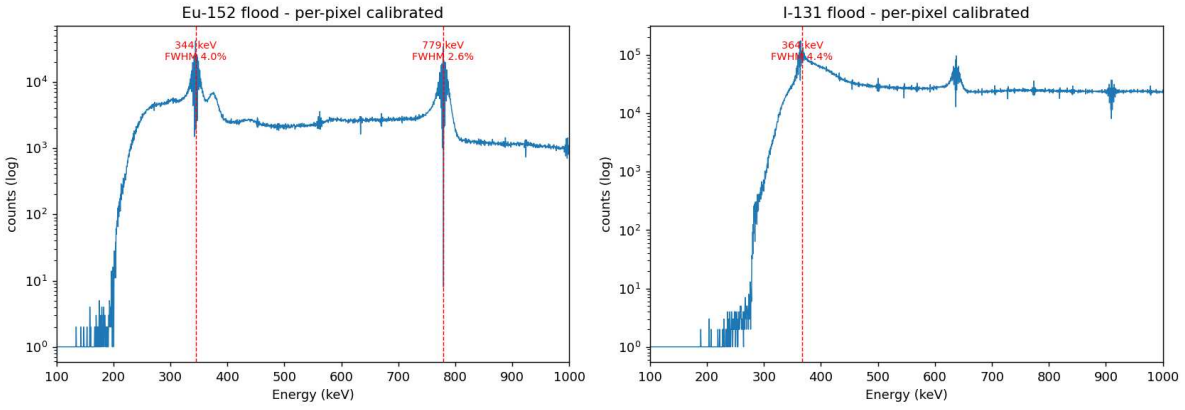
reconstruction [26–28]. Feasibility was established through Monte Carlo design studies, phantom measurements and a qualitative clinical comparison in thyroid patients, in which the diagnostic findings concurred with those of the commercial system. That work did not, however, quantify the detector's clinical performance reproducibly against the commercial reference's published specifications.

The present study sets out to close that gap. We characterise the SAIGC detector physics, covering energy resolution, noise, acquisition behaviour and intrinsic sampling, entirely from raw list-mode data, from bench sources and from patient acquisitions at clinical doses, and we benchmark the results against the published NEMA NU-1 specifications of the commercial camera. Dedicated source and phantom acquisitions then establish the camera's spatial, dual-isotope and tomographic capability, and clinical thyroid images from 30 patients imaged on both systems show that the studies it produces are clinically interpretable.

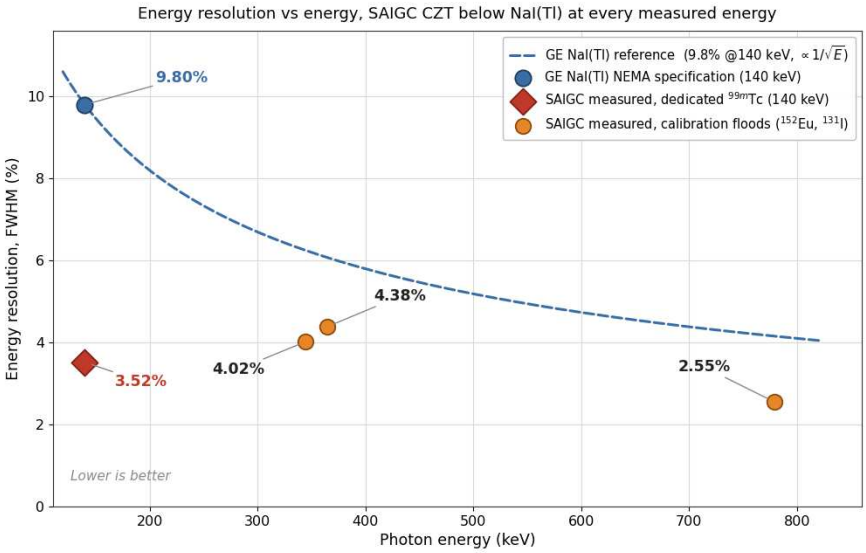
Results

Energy resolution

For SAIGC, a dedicated ^{99m}Tc acquisition gave an energy resolution of 3.52% FWHM at 140 keV, well below the 9.8% specified for the GE Infinia at this energy. In the source floods the resolution was 4.0% at 344 keV, 4.4% at 364 keV and 2.6% at 779 keV (^{152}Eu and ^{131}I; Figure 1(a)). The modest variation across these lines reflects the balance of electronic noise and charge-transport broadening, together with differences in flood statistics between acquisitions; the expected improvement toward higher energy is recovered at 779 keV. At every measured energy the CZT camera lies below the NaI(Tl) statistical-limit curve anchored to the 9.8% GE specification at 140 keV (Supplementary Table S4, Figure 1(b)). The finer resolution permits a narrower photopeak window, and with it the rejection of a greater fraction of Compton-scattered photons.



(a)



(b)

Figure 1.

Because the photopeak is this narrow, a tight energy window retains the full-energy events while rejecting most of the sub-photopeak continuum, which is the physical origin of the detector's scatter rejection. We quantified this directly from the ^{99m}Tc list-mode spectrum (Figure 2). The 140 keV photopeak (FWHM 3.52%) is superimposed on a continuum of down-scattered photons and detector-response events (Compton escape and inter-pixel charge sharing). Broadening the photopeak to the NaI(Tl) specification of 9.8% while holding this continuum fixed, thereby isolating the effect of energy resolution alone, reveals the penalty of coarser resolution: to retain 95% of photopeak events, a 9.8% GE camera requires an energy window approximately 2.8× wider than SAIGC (i.e. ±11 keV against ±4 keV for SAIGC) and its in-window scatter-and-background fraction is approximately 2.5× higher (27% against 11% for SAIGC). Scatter suppression in the count image therefore follows directly from the narrower window that the CZT resolution allows.

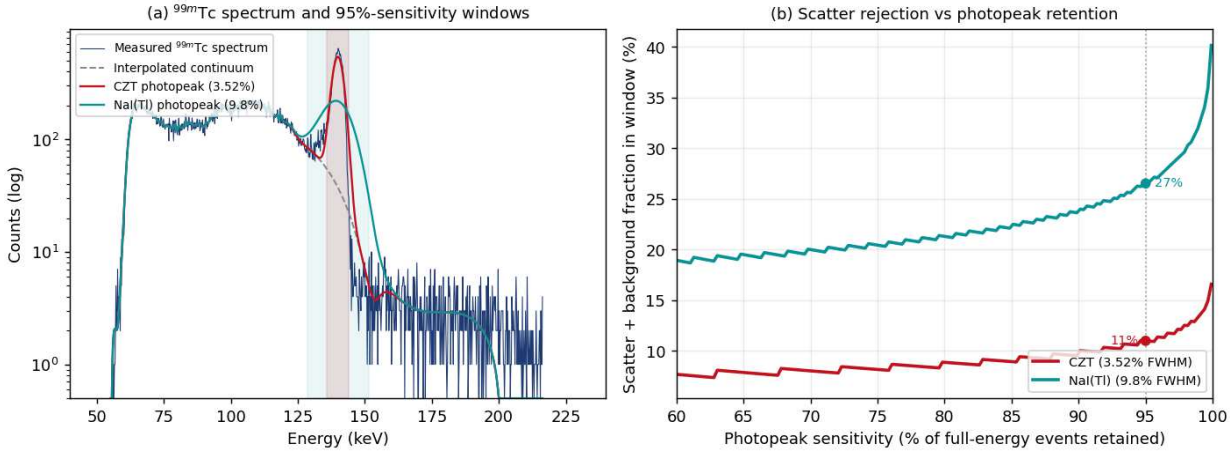


Figure 2.

Noise, acquisition, sensitivity and spatial sampling

Splitting each acquisition into alternate 100 ms blocks gave std(z) = 0.996 (95% CI 0.986 to 1.007; patient-level bootstrap over 11 patients, 20,306 pixel-measurements), consistent with the Poisson value of 1; the excess variance is at most 1.3% (95% upper limit). Across all 29 stationary acquisitions of the cohort the same statistic was 0.998 (95% CI 0.992 to 1.004). Because it compares interleaved short blocks, this statistic detects correlated counting within a pixel (duplicate counts in more than about 0.7% of events would have been detected) but is insensitive by design to slow changes in count rate. It did not depend on block duration from 1 ms to 300 ms; for blocks of 1 s and 5 s it rose in the full cohort (excess variance 1.4% and 3.9%), as slow positional changes in high-count acquisitions were no longer cancelled. The z distribution had skew −0.007 and excess kurtosis −0.146, consistent with the exact binomial expectation at these count levels (−0.09 ± 0.03), and its quantiles followed those of the exact binomial distribution across ±4σ (Figure 3). Over the nine acquisitions retained for it, the photon-transfer regression gave a slope of 0.990 (95% CI 0.980 to 1.011) and an intercept of 0.008 counts² (95% CI −0.003 to 0.019; wild cluster bootstrap over patients; joint test of unit slope and zero intercept, p = 0.32), and the pooled variance-to-mean ratio was 0.998 (95% CI 0.995 to 1.002). With the window placed on the 140 keV photopeak in every acquisition (Methods), the half-split gave the same result (std(z) = 1.002, 95% CI 0.992 to 1.011, 11 patients; 0.998, 95% CI 0.993 to 1.002, 29 acquisitions), whereas the variance-to-mean ratio of the eight acquisitions then retained for photon transfer was 1.029 (95% CI 1.011 to 1.051): the sharper photopeak image of the gland registers its slow changes in position (centroid shifts of up to 3.7 mm at the detector), which interleaving cancels (Supplementary Note 1). Each view required a median of 119.6 s (range 17.0 to 179.8 s) and yielded a median of 56,782 counts within ±5% of the 140 keV photopeak (range 7,624 to 348,771), giving a relative statistical noise of 0.42% at the median count, and a median photopeak rate of 529 cps. The patient-derived sensitivity was a median of 5.2 cps MBq^{-1} (interquartile range 2.4 to 14.5), computed against the measured net administered activity of 111 MBq, decay-corrected to the start of SAIGC imaging at approximately 41 min post-injection (102.6 MBq); it is reported solely as a measure of clinical count yield and is not comparable to the GE point-source NEMA sensitivity. Acquisitions were analysed over their artefact-free interval (Supplementary Note 1). The 2.0 mm anode pitch sets a sampling limit finer than the 3.8 mm (CFOV) intrinsic spatial resolution specified for the GE camera, although a sampling pitch and a measured FWHM are not equivalent quantities. Table 1 collates the specifications and the characterisation results.

Table 1.

Parameter	SAIGC (this work)	GE Infinia (NEMA / clinical)
Detector	Pixellated CZT (direct conversion)	NaI(Tl) + PMT (Anger)
Configuration / FOV	44×44 = 1936 anodes; 88×88 mm (SFOV)	LFOV; 540×400 mm UFOV
Detector element	2×2×5 mm; 50 µm gap	Monolithic crystal (3/8″)
Sampling pitch / intrinsic resolution	2.0 mm anode pitch	3.8 mm FWHM (CFOV)

Parameter	SAIGC (this work)	GE Infinia (NEMA / clinical)
Energy resolution @140 keV	3.52% FWHM (^{99m}Tc, dedicated); 4.0–4.4% at 344–364 keV	9.8% FWHM
Digitisation	12-bit list-mode (per-event E, t)	Windowed clinical image output
Count-rate capability	≈625 kcps sustained (40 kcps photopeak)	460 kcps (max)
Noise behaviour	Photon-noise-limited at the pixel level: half-split std(z) = 0.996 (95% CI 0.986 to 1.007); excess variance ≤ 1.3%	N/A
Median acquisition (this cohort)	119.6 s per view (range 17.0–179.8 s)	N/A
Thyroid collimation	Pinhole	LEHR
Approx. cost	≈₹40 lakh (₹4.0 million; ~US$42,000)	≈₹5 crore (₹50 million; ~US$530,000)

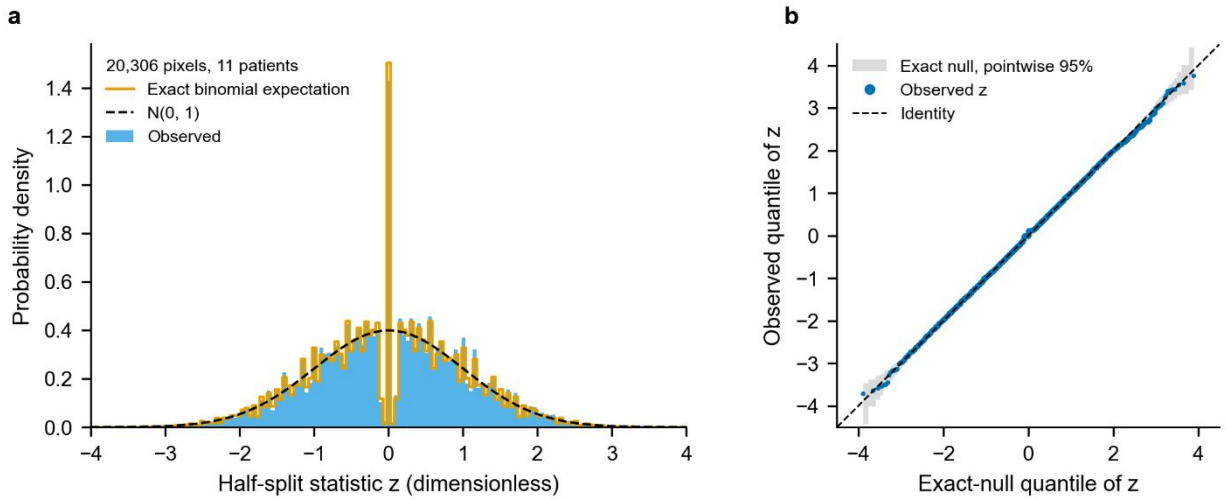


Figure 3.

Spatial discrimination and central-field response

The remaining characterisations used dedicated bench sources rather than patient data. These acquisitions map the spatial-separation behaviour of the detector (Supplementary Figure S6). A 6 mm diameter ^{131}I source was clearly resolved in the central field with little surrounding background, and a 15 mm ^{131}I line source preserved its shape and orientation. Two 3 mm sources imaged at the same time, ^{99m}Tc (25.9 MBq) and ^{131}I (37 MBq), were separated without appreciable overlap. An extended cross-shaped ^{131}I source produced a continuous, centrally peaked response with no dead regions across the central field. These acquisitions are qualitative; standardised NEMA point-source resolution and flood uniformity measurements remain to be performed.

Simultaneous dual-isotope imaging

With ^{152}Eu (122 keV) and ^{99m}Tc (140 keV) present in the field simultaneously, their photopeaks only 18 keV apart, the detector resolved the two radionuclides and rendered each distinctly in a single acquisition (Figure 4), a demanding test of spectral separation. The more widely separated ^{99m}Tc (140 keV) / ^{131}I (364 keV) pairing was resolved equally cleanly (Supplementary Figure S6(c)). Separation of this kind follows from the energy resolution of the detector and is a prerequisite for simultaneous dual-tracer protocols.

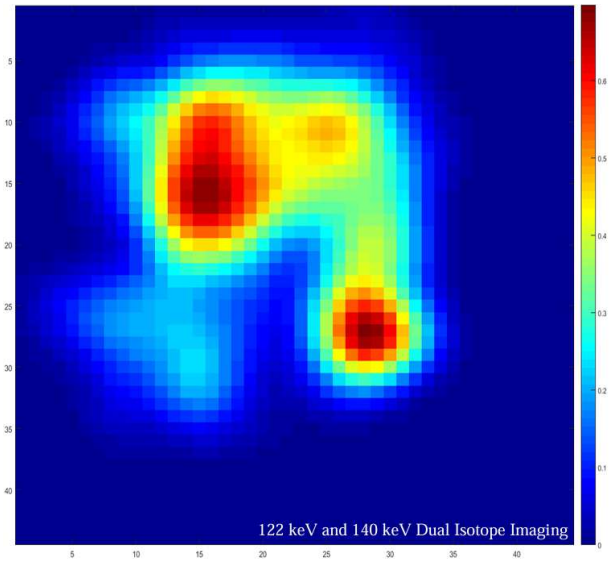


Figure 4.

Multi-angle acquisition and tomographic feasibility

A ^{99m}Tc-filled thyroid phantom was imaged over a full rotation, 0° to 360° in 30° increments (12 projections). The thyroid was identifiable in every projection (Figure 5), the lobes foreshortening and, in the lateral views, superimposing as the viewing geometry requires. A complete, self-consistent set of angular projections is a precondition for tomographic (SPECT) reconstruction, which makes a SPECT implementation the natural next step for this platform.

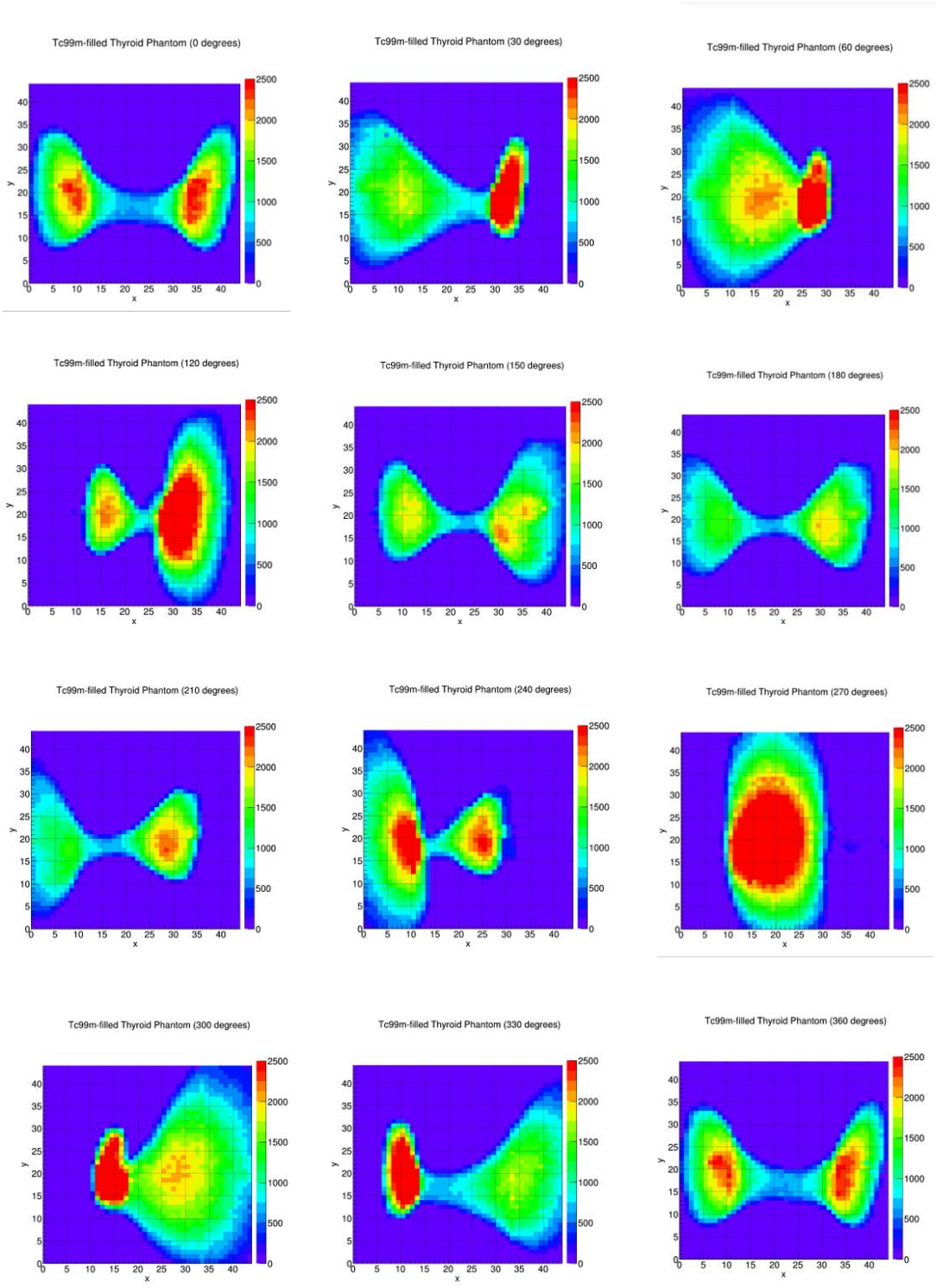


Figure 5.

Clinical demonstration

All 30 patients were imaged on both systems. The SAIGC studies were clinically interpretable: the two lobes and the overall uptake distribution were clearly depicted, and representative examples are shown in Supplementary Figure S7. The referring diagnoses spanned the usual range (Supplementary Table S2). Acquisition was rapid, with a median of 119.6 s per view, beginning immediately after the

21 min GE acquisition (approximately 41 min post-injection). Paired acquisitions from the two systems are presented together in Figure 6 for qualitative comparison.

GE Infinia (NaI(Tl))	SAIGC (CZT)

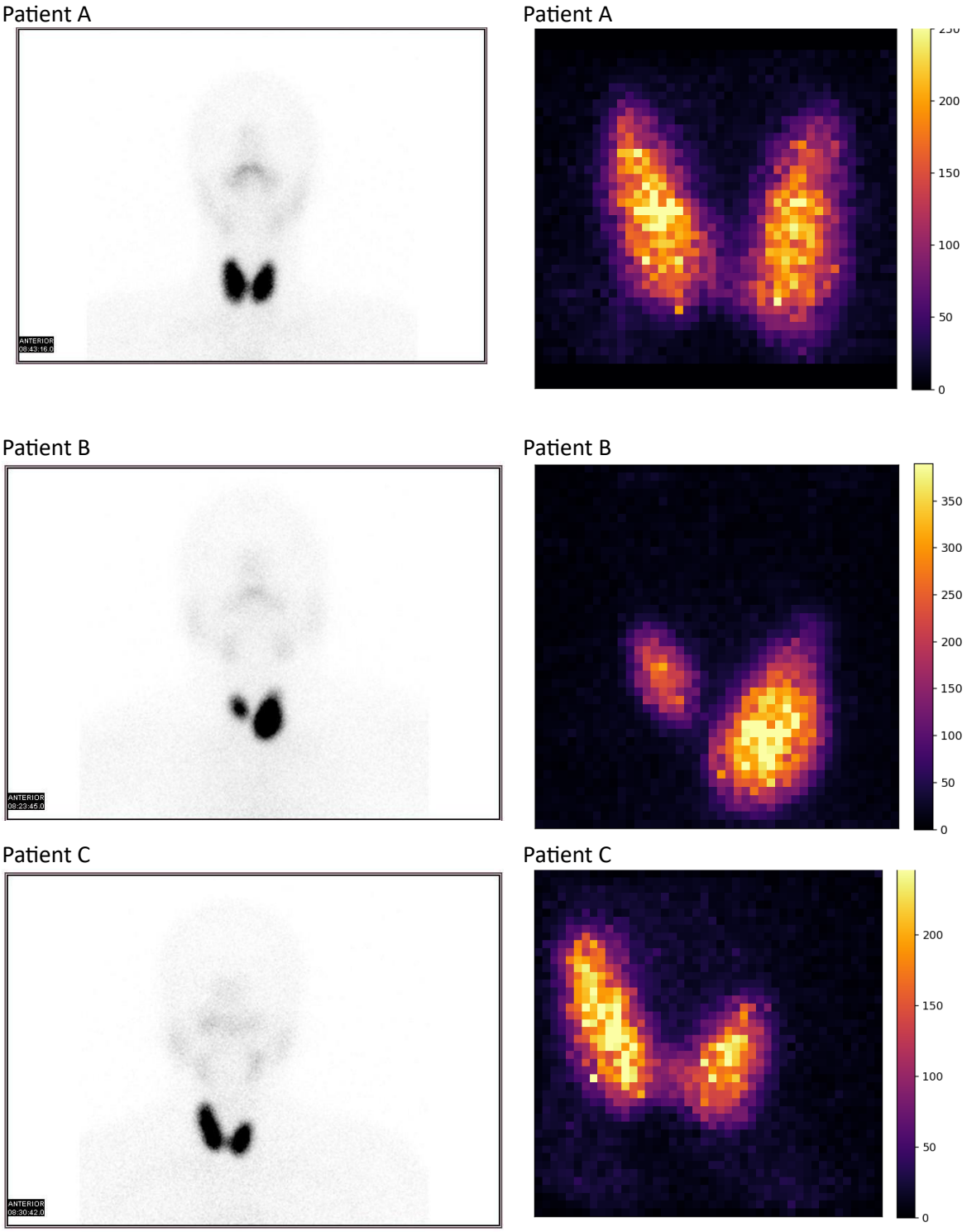


Figure 6.

Discussion

This study quantifies the performance of a low-cost direct-conversion CZT gamma camera and benchmarks it against the published specifications of a commercial NaI(Tl) system for planar thyroid scintigraphy. The findings that rest most securely on the raw data are the energy resolution, which is better than the comparator at every matched energy, and the noise behaviour, which is photon-limited. The 2.0 mm anode pitch also sets a sampling limit finer than the 3.8 mm intrinsic resolution quoted for the commercial camera. The energy-resolution advantage underlies the reduction in scatter admitted to the photopeak window, and on short timescales the pixel counts follow Poisson statistics, with no detectable correlated counting from the electronics.

These detector-physics results sit comfortably within the broader literature on direct-conversion semiconductor cameras. Compact CdTe and CZT cameras have repeatedly shown energy resolution superior to NaI(Tl) in sentinel-node and small-organ applications [11–13], and the values measured here, close to 4% FWHM at 344–364 keV and 3.52% at 140 keV, well below the 9.8% specification of the GE Infinia, are consistent with those reports. Earlier phantom work on this device [26] separated two 3 mm sources at 3 mm and resolved the 122 keV (^{152}Eu) and 140 keV (^{99m}Tc) photopeaks, 18 keV apart; the present acquisitions (Figure 4) reproduce that separation, consistent with the sampling and energy-resolution advantages reported here. Beyond those reports and the earlier qualitative assessment of the device, the present study adds a clinical patient cohort imaged on the camera, a reproducible detector-characterisation pipeline referenced to published NEMA specifications, and dual-isotope and tomographic capabilities.

The camera also has practical advantages. It is portable, it operates at room temperature, and it writes raw list-mode data that can be reconstructed and post-processed in any way the user chooses. Its bill of materials is approximately ₹40 lakh (₹4 million), against roughly ₹5 crore (₹50 million) for the commercial system, so about one-tenth the cost; at an exchange rate of ₹95 per US dollar these correspond to approximately US$42,000 and US$530,000 respectively. Separately, tomographic reconstruction on this platform has been ported to a field-programmable gate array: an FPGA implementation of the maximum-likelihood expectation-maximisation algorithm [29] achieved a reported speed-up of approximately 288× over a workstation CPU [27]. That result concerns tomographic reconstruction and is distinct from the planar acquisitions reported here. The sustained count-rate capability of approximately 625 kcps, taken from earlier device-level characterisation [26–28], also accommodates short acquisitions, consistent with the median of 119.6 s per view measured in this cohort.

The bench and phantom studies extend what has been demonstrated for the camera beyond the planar comparison, and are summarised in Supplementary Table S3. Two radionuclides were separated in a single acquisition even with photopeaks only 18 keV apart (^{152}Eu at 122 keV, ^{99m}Tc at 140 keV, Figure 4), and the widely spaced ^{99m}Tc/^{131}I pair was resolved as cleanly. A simultaneous dual-tracer protocol depends on exactly this kind of spectral discrimination, which arises from the CZT energy resolution. The point, line and dual-point source images confirm that closely spaced sources remain localised and separable, consistent with the fine anode sampling. A complete, shape-preserving 0–360° projection set of a thyroid phantom is a first step toward tomographic

reconstruction on this hardware, and with it a future SPECT capability. These results are qualitative in nature.

The detector-level comparison is referenced throughout to the published NEMA NU-1 specifications of the commercial system, which is the standardised framework by which clinical gamma cameras are specified, procured and accepted. This places both systems on common, internationally recognised axes while every SAIGC figure remains traceable to its own raw list-mode stream. Each quantity is also reported under the definition by which it was measured: the 140 keV energy resolution as a relative FWHM taken from a per-pixel-calibrated system spectrum, and the patient-derived sensitivity as a clinical count yield over the thyroid field rather than a NEMA point-source sensitivity. Reporting them in their native definitions keeps each number verifiable against the data behind it.

It is worth setting out what this characterisation covers and where it leads. The 88×88 mm field of view is matched by design to the thyroid and to the small-organ applications for which the camera was built, and the clinical studies used its pinhole collimator, with the custom LEHR parallel-hole collimator available where a wider field is required. The GE Infinia values above 140 keV were calculated from the GE Healthcare datasheet value (measured according to the NEMA NU 1 standard) using the counting-statistics relation (Eq. 3): NaI(Tl) carries additional non-statistical broadening, so the resolution margin reported here is, if anything, an underestimate of the true advantage. The clinical cohort establishes what a detector characterisation sets out to establish, namely that the camera yields interpretable planar thyroid studies at routine clinical activity levels, and it opens the way to a powered, blinded reader study.

In summary, this work provides a reproducible, raw-data characterisation of a low-cost, portable direct-conversion CZT gamma camera. Its energy resolution is 3.52% FWHM at 140 keV against 9.8% for the NaI(Tl) comparator, and it lies below the comparator's statistical-limit curve at every measured energy. On short timescales the pixel counts of the clinical acquisitions follow Poisson statistics, with no detectable correlated counting from the electronics. Photopeaks only 18 keV apart are discriminated in a single acquisition, and thyroid morphology is preserved across a full 0–360° rotation. These results are obtained at roughly one-tenth the cost of the commercial system and alongside clinically interpretable planar thyroid studies in thirty patients. Together they support indigenous, low-cost CZT gamma cameras as a practical basis for dedicated small-organ imaging.

Methods

The SAIGC

The SAIGC (Figure 7) is a pixellated CZT array of 44×44 = 1936 anodes, arranged as a 4×4 grid of CZT modules, each module spanning 11×11 anodes over 22×22 mm^2. Each element occupies a 2×2 mm cell in the imaging plane, including a 50 µm inter-anode gap, and is 5 mm deep; collectively they

subtend an 88×88 mm central field of view at a 2 mm anode sampling pitch. The 5 mm crystal depth affords adequate detection efficiency up to approximately 360 keV. A 12-bit ADC (channels 0–4095) digitises each event, and an all-digital list-mode acquisition system records one entry per detected photon. CZT was selected following a GEANT4 Monte Carlo comparison of NaI(Tl), $LaBr_3$ and CZT (Supplementary Figure S5) under matched conditions, in which CZT proved superior in detection efficiency, energy resolution and form factor, and cheaper to fabricate as a finely segmented crystal [26]. Two collimators are available for thyroid imaging: a pinhole for high resolution, and a custom lead low-energy high-resolution (LEHR) parallel-hole configuration for a wider field.



Figure 7.

Comparator system and basis of comparison

The comparator was a GE Infinia large field-of-view camera with a NaI(Tl) crystal, in routine clinical use for thyroid scintigraphy. Detector-level comparison was made against the manufacturer's published performance specifications [3], measured according to the NEMA NU-1 (2001) standard [30], which provides a standardised and widely accepted reference. For the standard 3/8" (9.5 mm) crystal these are: intrinsic energy resolution 9.8% FWHM at 140 keV; intrinsic spatial resolution 3.8 mm (CFOV) / 3.9 mm (UFOV); integral flood uniformity 3.0% (CFOV) / 3.6% (UFOV); and a maximum count rate of 460 kcps.

SAIGC detector performance was characterised from its raw list-mode data, which record the energy and timestamp of every detected event, and benchmarked against the GE NEMA specifications above. Clinical images acquired on both systems are presented to demonstrate clinically interpretable thyroid imaging; because clinical console images incorporate vendor-specific reconstruction and display processing, the quantitative comparison is based on raw-data detector metrics. Each patient received 111 MBq of ^{99m}Tc-pertechnetate. The net administered activity was established by imaging the loaded syringe for 30 s immediately before injection, the emptied syringe for 1 min afterwards and the injection site for 1 min, so that residual and extravasated activity could be subtracted from the loaded value; the thyroid was imaged last. The 111 MBq quoted throughout is this net figure. Beginning at 20 min post-injection, each patient was imaged on the GE Infinia for 21 min, followed immediately by

SAIGC imaging, with each SAIGC view requiring a median of 119.6 s, supporting a rapid acquisition workflow.

Patients and acquisition

Thirty consecutive patients referred for planar anterior thyroid scintigraphy were imaged on both systems at HCG Cancer Centre, Bengaluru. Each received the 111 MBq intravenous dose described above and was imaged 20 min later, first on the GE Infinia and subsequently on SAIGC. Collectively the cohort spanned the common thyroid presentations: Graves' disease, multinodular goitre and thyroiditis. The study was approved by the Institutional Ethics Committees of the Sri Sathya Sai Institute of Higher Learning and of HCG Hospital, Bengaluru. It was performed in accordance with the Declaration of Helsinki and with the guidelines of the Ministry of Health and Family Welfare, Government of India. Written informed consent was obtained from every participant before imaging.

The referring diagnoses were Graves' disease (n = 15), thyroiditis (n = 7), multinodular goitre (n = 2), euthyroid or normal studies (n = 3), a TSH-suppression effect (n = 2) and resolving thyroiditis (n = 1); Supplementary Table S2 summarises the cohort and the acquisition protocol, and per-patient age, sex and referring diagnosis are listed in Supplementary Table S1.

List-mode data and image reconstruction

Every detected photon is written as a 13-byte list-mode record carrying, among other fields, the anode pixel index (0–1935) and the 12-bit event energy; cathode and temperature pseudo-pixels are discarded. Images were reconstructed from these records following the detector's per-pixel energy calibration and flood correction. In brief: events within a ±5% window about each pixel's ^{99m}Tc photopeak were binned into a 44×44 count image, which was then corrected pixel-by-pixel with a median-normalised flood, and the small number of dead or out-of-tolerance pixels was replaced by neighbour-median interpolation. The parser and the pixel-to-position mapping were validated against the detector's own per-pixel spectra, with a Pearson correlation coefficient above 0.99 in both total counts and spectral shape.

Detector characterisation

Energy resolution. Each photopeak was fitted with a Gaussian on a linear background, and resolution reported as the FWHM relative to the photopeak centroid, in per cent. The high-energy points were obtained from prolonged uniform-flood exposures of ^{152}Eu (344.3 and 778.9 keV) and ^{131}I (364.5 keV); following the per-pixel calibration, the individual spectra were summed into a single system spectrum so that inter-module gain differences did not broaden the peaks. The dedicated 140 keV ^{99m}Tc acquisition was per-pixel calibrated and summed in the same way as the floods, so that its resolution is likewise a system figure; the value was read directly from the summed photopeak, whose maximum fell at channel 1420 with half-maximum points at channels 1397 and 1447, giving a 50-channel width and 50/1420 = 3.52% FWHM (channel-quantisation uncertainty ≈ ±0.07%), in agreement with the Gaussian-plus-linear fit (equations (1) and (2)). The channel-to-energy relation is linear with negligible zero-offset over this range. The ^{152}Eu and ^{131}I floods were acquired at a lower ADC gain than the dedicated ^{99m}Tc acquisition, so that the 779 keV line fell within the 12-bit range, and each acquisition was calibrated at its own gain. To place the NaI(Tl) camera on common axes, its single quoted 140 keV

value was scaled to the other energies via the counting-statistics relation R(E) ∝ 1/√E; because NaI(Tl) additionally carries non-statistical broadening, this scaling is a conservative bound for the comparator.

The peak model and the resulting width are

$$S(E) = A \exp\left[-\frac{(E - E_0)^2}{2\sigma^2}\right] + aE + b \tag{1}$$

$$\mathrm{FWHM} = 2\sqrt{2\ln 2}\,\sigma \approx 2.355\,\sigma, \quad R(\%) = 100 \times \frac{\mathrm{FWHM}}{E_0} \tag{2}$$

and the NaI(Tl) scaling is

$$R_{NaI}(E) = R_{NaI}(140)\sqrt{\frac{140}{E}} \tag{3}$$

Scatter rejection. NEMA NU-1 addresses scatter-related performance through separately defined tests, among them system spatial resolution with scatter, planar sensitivity with collimator penetration and scatter, and count-rate performance with scatter. None of these is a spectral measurement of scatter fraction against window width, so no standardised protocol exists for the comparison made here. Our approach follows the framework of Kojima et al. [15], who used Monte Carlo simulation of a ^{99m}Tc line source in a water phantom to show how detector energy resolution (8–16% FWHM at 140 keV) governs the trade-off between energy-window width (8–23%) and scatter fraction. We apply that relationship between resolution and scatter fraction to a measured rather than a simulated spectrum, using the dedicated ^{99m}Tc list-mode spectrum throughout. Its sub-photopeak continuum, which unlike an idealised Monte Carlo model contains detector-specific charge-sharing and escape events, was estimated by interpolating a smooth background beneath the 140 keV peak, and the fraction of in-window counts falling below the photopeak was computed from this fixed continuum. The continuum was then held constant while only the modelled photopeak width (Gaussian FWHM) was varied, so that the comparison isolates the effect of energy resolution on window width, and hence on admitted scatter, without altering the underlying scatter physics. The photopeak was broadened from the SAIGC resolution to the NaI(Tl) specification of 9.8%, and the two configurations were compared at matched photopeak sensitivity. This construction is an empirical, spectrum-based adaptation of the Kojima framework, combining standard Gaussian photopeak modelling with continuum interpolation beneath the peak. It is mechanistically distinct from image-domain scatter-correction methods such as dual- or triple-energy-window correction [31,32], which use narrow flanking windows to estimate and subtract scatter pixel by pixel in a reconstructed image rather than to compare the intrinsic resolution of two detectors on a raw spectrum.

Noise. In a photon-counting detector, readout noise appears mainly as spectral broadening and can enter the count image only as non-Poisson fluctuation of the counts. To test for correlated counting within pixels, each acquisition was partitioned into two half-samples by time: the list-mode stream was divided into contiguous blocks of duration Δ = 100 ms and alternate blocks were assigned to sub-images A and B, over an even number of complete blocks so that the two exposures are exactly equal. Absolute event times were reconstructed from the per-module 16-bit timestamp by cumulative wrap counting. Each acquisition's duration was taken as the median of the sixteen module spans; these

agreed to within 0.02% in nine of the first twelve acquisitions, while in the three lowest-count acquisitions modules that were silent for longer than one 65.536 ms counter period lost that period, shortening their reconstructed spans by up to 2.4 s, with no measurable effect on the statistics below (module-by-slice χ^2 test, $p \geq 0.16$). For a homogeneous Poisson process the arrival times conditional on the total count are independent and uniform, so each event enters A with probability one half and the normalised difference

$$z = \frac{N_A - N_B}{\sqrt{N_A + N_B}}, \qquad Var(z) = 1 \tag{4}$$

has unit variance; $std(z)$ close to unity therefore indicates that the noise is essentially all photon noise, with no measurable correlated counting within a pixel. A temporal rather than per-event split is required: partitioning recorded events at random satisfies $Var(z) = 1$ identically, for any detector, and so carries no information. The temporal split was verified to be two-sided and sensitive against simulated dead time ($std(z) = 0.823$ at 20% dead fraction) and clustered arrivals ($std(z) = 1.410$), and to return 1.002 for Poisson arrivals. As an independent check, each acquisition was also divided into forty equal time slices and the per-pixel variance across slices was regressed on the per-pixel mean; for Poisson counting this relation has unit slope and zero intercept, and the pooled variance-to-mean ratio, the sum of the per-pixel variances divided by the sum of the per-pixel means, summarises it in one number. Events were taken within ±5% of the channel at which each acquisition's energy spectrum peaked. In 13 acquisitions this is the 140 keV photopeak; in the other 17 the spectral maximum, and with it the window, lies on the low-energy continuum just above the acquisition threshold, although the photopeak occupies the same channels in all thirty (Supplementary Note 1). Because the half-split concerns the arrival statistics of the counted events rather than their energy, the analysis was also repeated with the window on the photopeak in every acquisition (Results). Each acquisition was first screened second by second for count-rate anomalies and analysed from its start to the last second before the first run of at least three anomalous seconds (three acquisitions were shortened; Supplementary Note 1). Uncertainties were computed at the patient level, because pixels within an acquisition are not independent: patient bootstrap intervals (10,000 resamples) for std(z) and the variance-to-mean ratio, and wild cluster bootstrap intervals (Webb weights, 9,999 resamples) for the regression coefficients. Acquisitions were excluded by two rules set during the analysis of the first twelve acquisitions and applied unchanged to all thirty: as non-stationary if their Fano factor exceeded 10 (one acquisition, in which one detector module recorded a 16 s burst of low-amplitude events during the final 20 s), and from the photon-transfer regression only if their peak mean exceeded 10 counts per pixel per slice (two of the first twelve acquisitions). In both of the latter the slice-to-slice excess is a redistribution of counts within the image, consistent with a gradual displacement of the gland image of about 3 to 4 mm at the detector; measured photopeak drift accounts for at most 2% of it. Their half-split statistics, which cancel slow changes by interleaving, are retained (Supplementary Note 1).

Sensitivity and acquisition. From the list-mode stream we tabulated the duration of each view and the count rate within ±5% of the 140 keV photopeak. A patient-derived sensitivity, defined as photopeak counts per second per unit decay-corrected administered activity, is also reported. This is not a NEMA sensitivity. Only the thyroid uptake and some adjacent neck activity lie within the field of

view, rather than the whole administered dose, and the pinhole geometry differs fundamentally from the NEMA point-source configuration. The value should be read as a clinical count yield.

Spatial sampling. The 2 mm anode pitch sets an intrinsic sampling limit. We compare it with the NEMA intrinsic spatial resolution of the GE camera, noting that a sampling pitch and a measured FWHM are not equivalent quantities.

Phantom and source-imaging studies. The detector was further characterised with a series of source and phantom acquisitions across the 44×44 anode array. For spatial discrimination we imaged a 6 mm diameter ^{131}I source and a 15 mm ^{131}I line source in the central field, together with a pair of 3 mm sources, namely ^{99m}Tc (25.9 MBq) and ^{131}I (37 MBq), imaged side by side in a single acquisition. A cross-shaped ^{131}I source probed response uniformity across that central field. To assess simultaneous dual-isotope separation we co-imaged ^{152}Eu (122 keV) with ^{99m}Tc (140 keV), separated by only 18 keV, and, separately, ^{99m}Tc (140 keV) with ^{131}I (364 keV). Finally, a ^{99m}Tc-filled thyroid phantom was imaged over a full rotation, 0° to 360° in 30° increments (12 projections), to evaluate the feasibility of a tomographic acquisition.

Reproducibility

The entire pipeline is scripted and executed in Python 3.11.4 (NumPy 1.26, SciPy 1.16, scikit-image 0.21, statsmodels 0.14, pingouin 0.6, Pillow 11.3, scikit-learn 1.8, Matplotlib 3.7). Absolute event times for the noise analysis were reconstructed from the per-module 16-bit list-mode timestamp by cumulative wrap counting, with acquisition durations taken as the median of the sixteen module spans and checked against acquisitions of known nominal duration. The intermediate outputs, comprising per-patient event summaries and the figure data, are retained so that the analysis can be reproduced end to end.

Data availability

The list-mode datasets generated and analysed during the current study are not publicly available, because the ethics approval and patient consent obtained do not extend to public release of patient-derived data, but de-identified list-mode files are available from the corresponding author on reasonable request. The bench source, flood and phantom acquisitions used for detector characterisation, and the list-mode parsing, event-time reconstruction and noise-analysis scripts underlying Supplementary Note 1, are also available from the corresponding author on reasonable request.

References

1. Anger, H. O. Scintillation camera. Rev. Sci. Instrum. 29, 27–33 (1958).
2. Madsen, M. T. Recent advances in SPECT imaging. J. Nucl. Med. 48, 661–673 (2007).
3. GE Healthcare. Infinia Product Data, Release 2.5, Direction 2411980-100 Rev. 3 (GE Healthcare, 2006).
4. Hurwitz, S. R., Ashburn, W. L., Green, J. P. & Halpern, S. E. Clinical applications of a “portable” scintillation camera. J. Nucl. Med. 14, 585–587 (1973).

5. Perkins, A. C. & Hardy, J. G. Intra-operative nuclear medicine in surgical practice. Nucl. Med. Commun. 17, 1006–1015 (1996).
6. Goertzen, A. L., Thiessen, J. D., McIntosh, B., Simpson, M. J. & Schellenberg, J. Characterization of a handheld gamma camera for intraoperative use for sentinel lymph node biopsy. In 2013 IEEE Nuclear Science Symposium and Medical Imaging Conference (NSS/MIC) 1–4 (IEEE, 2013).
7. Mathelin, C., Salvador, S., Huss, D. & Guyonnet, J.-L. Precise localization of sentinel lymph nodes and estimation of their depth using a prototype intraoperative mini γ-camera in patients with breast cancer. J. Nucl. Med. 48, 623–629 (2007).
8. Ortega, J., Ferrer-Rebolleda, J., Cassinello, N. & Lledó, S. Potential role of a new hand-held miniature gamma camera in performing minimally invasive parathyroidectomy. Eur. J. Nucl. Med. Mol. Imaging 34, 165–169 (2007).
9. Lees, J. E., Bassford, D. J., Blake, O. E., Blackshaw, P. E. & Perkins, A. C. A high resolution small field of view (SFOV) gamma camera: a columnar scintillator coated CCD imager for medical applications. J. Instrum. 6, C12033 (2011).
10. Darambara, D. G. & Todd-Pokropek, A. Solid state detectors in nuclear medicine. Q. J. Nucl. Med. 46, 3–7 (2002).
11. Tsuchimochi, M. et al. A prototype small CdTe gamma camera for radioguided surgery and other imaging applications. Eur. J. Nucl. Med. Mol. Imaging 30, 1605–1614 (2003).
12. Tsuchimochi, M., Hayama, K., Oda, T., Togashi, M. & Sakahara, H. Evaluation of the efficacy of a small CdTe γ-camera for sentinel lymph node biopsy. J. Nucl. Med. 49, 956–962 (2008).
13. Abe, A. et al. Performance evaluation of a hand-held, semiconductor (CdZnTe)-based gamma camera. Eur. J. Nucl. Med. Mol. Imaging 30, 805–811 (2003).
14. Russo, P. et al. Imaging performance comparison between a LaBr3:Ce scintillator based and a CdTe semiconductor based photon counting compact gamma camera. Med. Phys. 36, 1298–1317 (2009).
15. Kojima, A., Matsumoto, M., Takahashi, M. & Uehara, S. Effect of energy resolution on scatter fraction in scintigraphic imaging: Monte Carlo study. Med. Phys. 20, 1107–1113 (1993).
16. Hutton, B. F., Buvat, I. & Beekman, F. J. Review and current status of SPECT scatter correction. Phys. Med. Biol. 56, R85–R112 (2011).
17. Zaidi, H. & Koral, K. F. Scatter modelling and compensation in emission tomography. Eur. J. Nucl. Med. Mol. Imaging 31, 761–782 (2004).
18. Takahashi, T. & Watanabe, S. Recent progress in CdTe and CdZnTe detectors. IEEE Trans. Nucl. Sci. 48, 950–959 (2001).
19. Schlesinger, T. E. et al. Cadmium zinc telluride and its use as a nuclear radiation detector material. Mater. Sci. Eng. R Rep. 32, 103–189 (2001).
20. Del Sordo, S. et al. Progress in the development of CdTe and CdZnTe semiconductor radiation detectors for astrophysical and medical applications. Sensors 9, 3491–3526 (2009).
21. Iniewski, K. CZT detector technology for medical imaging. J. Instrum. 9, C11001 (2014).
22. Verger, L. et al. Characterization of CdTe and CdZnTe detectors for gamma-ray imaging applications. Nucl. Instrum. Methods Phys. Res. A 458, 297–309 (2001).

23. Barrett, H. H., Eskin, J. D. & Barber, H. B. Charge transport in arrays of semiconductor gamma-ray detectors. Phys. Rev. Lett. 75, 156–159 (1995).
24. Erlandsson, K., Kacperski, K., van Gramberg, D. & Hutton, B. F. Performance evaluation of D-SPECT: a novel SPECT system for nuclear cardiology. Phys. Med. Biol. 54, 2635–2649 (2009).
25. Tsuchimochi, M. & Hayama, K. Intraoperative gamma cameras for radioguided surgery: technical characteristics, performance parameters, and clinical applications. Phys. Med. 29, 126–138 (2013).
26. Ravi, M. & Sanagapati, S. S. S. A practical design and implementation of a low-cost platform for real-time diagnostic imaging. IEEE Access 5, 24952–24958 (2017).
27. Ravi, M., Sewa, A., Shashidhara, T. G. & Sanagapati, S. S. S. FPGA as a hardware accelerator for computation intensive maximum likelihood expectation maximization medical image reconstruction algorithm. IEEE Access 7, 111727–111735 (2019).
28. Ravi, M., Shashidhara, T. G., Sivaramakrishnan, S. & Sanagapati, S. S. S. A novel system on chip design for thyroid imaging studies. In 2016 IEEE International Conference on Advances in Electronics, Communication and Computer Technology (ICAECCT) 150–156 (IEEE, 2016).
29. Shepp, L. A. & Vardi, Y. Maximum likelihood reconstruction for emission tomography. IEEE Trans. Med. Imaging 1, 113–122 (1982).
30. National Electrical Manufacturers Association. NEMA Standards Publication NU 1-2001: Performance Measurements of Scintillation Cameras (NEMA, 2001).
31. Jaszczak, R. J., Greer, K. L., Floyd, C. E., Harris, C. C. & Coleman, R. E. Improved SPECT quantification using compensation for scattered photons. J. Nucl. Med. 25, 893–900 (1984).
32. Ogawa, K., Harata, Y., Ichihara, T., Kubo, A. & Hashimoto, S. A practical method for position-dependent Compton-scatter correction in single photon emission CT. IEEE Trans. Med. Imaging 10, 408–412 (1991).

Acknowledgements. This work was funded by the Department of Science and Technology (DST), Government of India, under project sanction no. DST/TSG/NTS/2015/67-G. The authors thank the Department of Molecular Medicine, HCG Cancer Centre, Bengaluru, for clinical acquisition support.

Author contributions. M.R. conceived and designed the study; K.V. performed the data acquisition and analysis; V.R. supervised the clinical studies and patient imaging at HCG Cancer Centre; all authors reviewed and approved the manuscript.

Competing interests. An Indian product patent application titled “Small Area Imaging Gamma Camera” has been filed by Sri Sathya Sai Institute of Higher Learning (Application No. 201941036983). The authors declare no other competing interests.

Figure and table legends

Figure 1. (a) (top) Energy-calibrated system spectra of the ^{152}Eu (left) and ^{131}I (right) uniform floods, with Gaussian-plus-linear photopeak fits. Fitted FWHM% values are annotated. The low-energy roll-off reflects the acquisition energy threshold, which removes the 122/140 keV region from the flood spectra; the 140 keV resolution was instead measured from a dedicated ^{99m}Tc acquisition (Supplementary Table S4). (b) (bottom) Energy resolution (FWHM%) versus photon energy. The SAIGC 140 keV point (3.52%, diamond) is from a dedicated ^{99m}Tc acquisition; the 344/364/779 keV points

are from ^{152}Eu and ^{131}I source floods. All SAIGC values lie below the NaI(Tl) statistical-limit reference ($R(E) \propto 1/\sqrt{E}$) anchored to the GE NEMA specification of 9.8% at 140 keV. Lower is better.

Figure 2. Scatter rejection from energy resolution (^{99m}Tc list-mode spectrum). (a) Measured spectrum with sub-photopeak continuum (dashed) and 140 keV photopeak modelled at SAIGC (3.52% FWHM) and NaI(Tl) (9.8% FWHM) resolution; shaded bands show 95%-retention windows. (b) In-window sub-photopeak fraction (scatter + detector background) versus photopeak sensitivity as window width varies. At 95% retention, the scatter/background fraction in the NaI(Tl) window is ~2.5× that in the CZT window.

Figure 3. (**a**) Distribution of the half-split statistic z over 20,306 pixel-measurements from 11 patients (bars), with the exact binomial expectation for the observed counts (orange) and the standard normal distribution (dashed); the spike at z = 0 and the gaps beside it arise because z takes discrete values at low counts. std(z) = 0.996 (95% CI 0.986 to 1.007, patient-level bootstrap); excess variance at most 1.3% (95% upper limit). (**b**) Quantiles of the observed z against those of the exact binomial distribution, with the pointwise 95% range of 400 data sets simulated under that distribution (grey); skew −0.007, excess kurtosis −0.146 (exact expectation −0.09). Derivation, controls, per-subject results and the full-cohort analysis are given in Supplementary Note 1.

Figure 4. Simultaneous dual-isotope imaging of ^{152}Eu (122 keV) and ^{99m}Tc (140 keV), whose photopeaks are separated by 18 keV. Both sources are distinctly resolved in a single acquisition, illustrating the spectral discrimination that follows from the detector's energy resolution.

Figure 5. Planar projections of a ^{99m}Tc-filled thyroid phantom over a full rotation (0–360°, 30° steps, 12 projections): (top) 0°, 30°, 60°, 120°, 150° and 180°; (bottom) 210–360°, where 360° repeats 0°. The thyroid is identifiable at every projection, the lobes foreshortening and superimposing consistently with viewing direction, as tomographic reconstruction requires. Colour scale: counts per pixel.

Figure 6. Representative paired clinical studies acquired on the GE Infinia (NaI(Tl), left) and SAIGC (CZT, right) for the same patients, shown for qualitative comparison.

Figure 7. SAIGC: a mobile, real-time planar gamma-imaging unit built around the pixellated CZT detector (44×44 = 1936 anodes, 2×2×5 mm elements, 88×88 mm field of view).

Table 1. SAIGC and GE Infinia: system specifications and detector-characterisation summary. SAIGC energy resolution, noise, acquisition and sensitivity were measured in this study; the count-rate figure is taken from earlier device-level characterisation [26–28]. GE figures are the manufacturer's NEMA NU-1 specifications [3]. Cost figures are approximate and based on bill of materials. The SAIGC entry under 'sampling pitch / intrinsic resolution' is the detector anode pitch, an intrinsic sampling limit, whereas the GE entry is a measured intrinsic spatial resolution (FWHM); the two are related but not directly equivalent. SFOV, small field of view; LFOV, large field of view; CFOV, central field of view; UFOV, useful field of view; LEHR, low-energy high-resolution; BOM, bill of materials.

Supplementary Files

This is a list of supplementary files associated with this preprint. Click to download.

- SupplementaryInformation.docx